

# Slip System Analysis of Magnesium Alloy AZ31B in Warm Compression by Visco-Plastic Self-Consistent Simulation<sup>\*1</sup>

Yusuke Matsuoka<sup>1,2,\*2,\*3</sup>, Mingzhe Bian<sup>2</sup>, Yuhki Tsukada<sup>1</sup>, Toshiyuki Koyama<sup>1,\*3</sup> and Yasumasa Chino<sup>2</sup>

<sup>1</sup>Department of Materials Design Innovation Engineering, Graduate School of Engineering, Nagoya University, Nagoya 464-8603, Japan

<sup>2</sup>Multi-Material Research Institute, National Institute of Advanced Industrial Science and Technology (AIST), Nagoya 463-8560, Japan

The active deformation mode (slip systems and twinning) of extruded AZ31B alloy (Mg-3Al-1Zn, mass%) during compression at RT, 100°C and 150°C was investigated by visco-plastic self-consistent (VPSC) simulation. Compression tests were first performed to obtain compression curve of AZ31B. The VPSC model was fitted to the compression curves to estimate the Voce hardening parameters which are required for the VPSC simulation. In the case of compression along the extrusion direction, work-hardening occurred rapidly with the transition of dominant deformation modes at all temperatures. In the case of compression to the other directions, basal  $\langle a \rangle$  slip was dominant throughout the deformation at all compression temperatures. In addition, prismatic  $\langle a \rangle$  slip and tensile twin were active in the early stage of deformation, and pyramidal  $\langle c + a \rangle$  slip became active in the later stage of deformation. Pyramidal  $\langle c + a \rangle$  slip became more active with increasing temperature from RT to 100°C, whereas basal  $\langle a \rangle$  and prismatic  $\langle a \rangle$  slips became more active with increasing temperature from 100°C to 150°C. These different trends in the change of the active slip system with increasing temperature can be attributed to the CRSS maximum of the pyramidal  $\langle c + a \rangle$  slip located around 100°C. [doi:10.2320/matertrans.MT-L2026001]

(Received February 11, 2026; Accepted March 25, 2026; Published June 25, 2026)

**Keywords:** magnesium alloy, deformation, simulation, parameter estimation

## 1. Introduction

As the lightest structural metal, magnesium (Mg) alloys are expected to be employed in a wide variety of applications, ranging from automotive body panels to housings for portable electronic devices [1, 2]. However, the hexagonal close-packed (HCP) crystal structure of Mg causes challenges in activating slip systems other than basal  $\langle a \rangle$  slip at room temperature, preventing the attainment of the five independent slip systems required for homogeneous deformation and resulting in poor room-temperature formability [3]. In contrast, at moderately elevated temperatures, non-basal slip modes such as prismatic  $\langle a \rangle$  slip and pyramidal  $\langle c + a \rangle$  slip become readily active, which improves formability [3, 4]. Consequently, industrial formation processes are often implemented in the warm-working regime at  $\sim 250^\circ\text{C}$  to secure the necessary formability [5–7]. In terms of energy consumption, however, warm-working is less favorable than cold-working and the processing temperature should be lowered to  $< 250^\circ\text{C}$ —i.e., to the sub-warm range ( $\approx 100$ – $150^\circ\text{C}$ ) or ultimately to room temperature. In this context, elucidating the plastic deformation behavior and activity of slip systems in the subwarm regime of Mg alloys is of clear engineering relevance.

Nevertheless, quantitative investigations of the frequency of individual slip system activation are intrinsically complex, and reports on subwarm deformation of Mg alloys are far fewer than those at room or high temperatures. To the best of our knowledge, although a few studies have examined rolled Mg sheets [8, 9], a quantitative analysis of slip-system activity in extruded Mg material within the sub-warm

temperature range has not yet been reported despite its practical importance.

Therefore, the present work is focused on the visco-plastic self-consistent (VPSC) simulation, which has been reported for room-temperature deformation-mechanism analysis in previous studies [8–13]. This simulation framework incorporates the activity of multiple deformation modes (slip systems and twinning), the associated crystallographic rotation, and the strain-hardening behavior of each mode, allowing the quantitative extraction of the activity level of each deformation mechanism [14].

In this study, the commercial AZ31B magnesium alloy is investigated. Compression tests are performed at room temperature and in the sub-warm range (100– $150^\circ\text{C}$ ). By applying VPSC simulations to these data, we aim to quantitatively elucidate how the compression direction and temperature affect the active slip systems during warm-working of extruded AZ31B. Moreover, we experimentally examine whether phenomena that are difficult to include in VPSC—namely, dynamic recrystallization and grain-boundary sliding [8, 9, 15]—occur during compression in the sub-warm regime.

## 2. Methods

The extruded AZ31B alloy (Mg, 3.0 mass% Al, 0.9 mass% Zn, and 0.3 mass% Mn) was sectioned into cubes with a side length of 3 mm so that the faces of each cube were oriented parallel to the extrusion direction (ED), transverse direction (TD), and normal direction (ND). Compression tests were conducted on these specimens at room temperature,  $100^\circ\text{C}$ , and  $150^\circ\text{C}$ , with a constant strain rate of  $1\text{ mm min}^{-1}$ . The termination criterion for each compression run was based on the load-cell capacity of the testing machine. To minimize friction, a thin layer of mechanical oil was applied between the specimens and the platens. The microstructures were examined using a JEOL scanning

<sup>\*1</sup>This Paper was Originally Published in Japanese in J. JILM 74 (2024) 73–82.

<sup>\*2</sup>Graduate Student, Nagoya University. Corresponding author, E-mail: matsuoka.yusuke@nims.go.jp

<sup>\*3</sup>Present address: Research Center for Structural Materials, National Institute for Materials Science (NIMS)

electron microscope (JSM-IT500) equipped with an electron back-scatter diffraction (EBSD) detector. The acquired EBSD patterns were automatically indexed and analyzed using OIM Analysis 7.0, from which inverse pole figure (IPF) maps were generated to assess the texture and grain structure before and after compression. Kernel average misorientation (KAM) maps were produced to evaluate the presence or absence of dynamic recrystallization in the compressed samples.

VPSC simulations were performed to analyze the active slip systems. In this model, the contributions of multiple deformation modes, along with the associated crystallographic rotations and strain hardening for each mode, were considered when calculating the macroscopic plastic response. The deviatoric strain-rate tensor of an individual grain,  $\dot{\varepsilon}_{ij}$ , follows the constitutive relation derived from crystal-plasticity theory and can be expressed as the sum of the strain-rate contributions from all active deformation systems,  $S$  [14, 16]:

$$\dot{\varepsilon}_{ij} = \sum_S m_{ij}^S \dot{\gamma}^S = \dot{\gamma}_0 \sum_S m_{ij}^S \left( \frac{m_{kl}^S \sigma_{kl}}{\tau^S} \right)^n, \quad (1)$$

where  $m_{ij}^S$  denotes the Schmid tensor of system  $S$ ,  $\dot{\gamma}^S$  is the shear rate on that system,  $\dot{\gamma}_0$  is a reference shear-rate (normalization factor),  $\sigma_{kl}$  is the deviatoric stress tensor,  $\tau^S$  is the critical resolved shear stress (CRSS) for system  $S$ , and  $n$  is the strain-rate-sensitivity exponent.

In the present work, the following four deformation modes were considered: basal  $\langle a \rangle$  slip  $\{0002\}\langle 11\bar{2}0 \rangle$ , prismatic  $\langle a \rangle$  slip  $\{1\bar{1}00\}\langle 11\bar{2}0 \rangle$ , pyramidal II  $\langle c + a \rangle$  slip  $\{11\bar{2}2\}\langle 11\bar{2}\bar{3} \rangle$ , and tensile twinning  $\{10\bar{1}2\}\langle 10\bar{1}1 \rangle$ . The strain-rate-sensitivity exponent was taken as  $n = 20$  based on previous studies [8, 9, 15], and the reference shear rate was set to  $\dot{\gamma}_0 = 1 \text{ s}^{-1}$ .

In the VPSC model, Eq. (1) was linearized for the numerical calculations, and several linearization schemes have been proposed. In the present study, we adopted linearization with the effective exponent,  $n_{\text{eff}} = 10$  [13], which has been shown to reproduce the plastic deformation behavior of Mg alloys relatively well [17]. The evolution of the CRSS for each deformation mode as a function of the accumulated shear strain,  $\Gamma$ , in a grain was described as per the Voce-type hardening law [18]:

$$\tau^S = \tau_0^S + (\tau_1^S + \theta_1^S \Gamma) \left[ 1 - \exp\left(-\frac{\theta_0^S \Gamma}{\tau_1^S}\right) \right], \quad (2)$$

where  $\tau_0^S$  is the initial CRSS,  $\tau_1^S$  is the back-extrapolated stress,  $\theta_0^S$  is the initial hardening rate, and  $\theta_1^S$  is the asymptotic hardening rate.

The predominant twin reorientation scheme [19] was employed to account for the crystallographic reorientation caused by twinning. At each increment, the twin volume fraction calculated from the shear contribution of twinning was compared with the threshold value,  $V^{\text{th,mode}}$ . When the threshold was exceeded, the orientation of the affected grain was instantaneously rotated to the twin orientation. The threshold is defined as follows:

$$V^{\text{th,mode}} = A^{\text{th1}} + A^{\text{th2}} \frac{V^{\text{eff,mode}}}{V^{\text{acc,mode}}}, \quad (3)$$

where  $V^{\text{eff,mode}}$  is the effective twin volume fraction of the mode,  $V^{\text{acc,mode}}$  is the accumulated twin volume fraction, and

the material constants are set to  $A^{\text{th1}} = 0.1$  and  $A^{\text{th2}} = 0.8$  (independent of temperature), as in previous work [8, 9].

To perform plastic-deformation simulations with the VPSC framework, both the initial texture and a set of Voce-hardening parameters for each deformation mode,  $(\tau_0^S, \tau_1^S, \theta_0^S, \theta_1^S)$ , are required. In the present study, the initial texture was directly derived from EBSD measurements performed on the specimens prior to compression, thereby providing a realistic description of the pre-deformed microstructure.

By contrast, the Voce-hardening parameters are intrinsic material constants that are not known a priori. Consequently, we adopted the parameter identification procedure proposed by Matsuoka *et al.* [10], which determines the Voce parameters by fitting the simulated compression curves to the experimentally measured ones. The fitting employed the compression data obtained along with the extrusion ED, TD, and ND for each temperature. The parameter set that yielded the best agreement between the simulated and experimental stress-strain curves was selected as the solution for that temperature.

To assess the uniqueness of the identified parameters and the reliability of the subsequent analysis, we performed a statistical robustness check. The initial guess for the optimization was generated by perturbing the room-temperature values reported for AZ31 [17] by a random factor within  $\pm 50\%$  and then running the fitting routine 32 independent times for each temperature.

### 3. Results

Figure 1 shows the IPF map obtained from EBSD for the undeformed specimen, along with the corresponding pole figures of the initial texture. The average grain size of the material used in this study was  $46.9 \mu\text{m}$ , resulting in a fully recrystallized microstructure composed of relatively coarse grains. In addition, the texture was confirmed to be the typical one for Mg-extruded sheets, in which the  $\{0002\}$  basal-plane normals are oriented perpendicular to the ED [20].

Figures 2(a)–2(c) present the results of the compression tests conducted in this study, separated according to the loading direction: ED, TD, and ND. In all cases, the specimens retained an almost rectangular shape after testing, and the effect of barreling was negligible; therefore, the deformation can be regarded as homogeneous. Among the three loading directions, compression along TD or ND shows gradual work-hardening after yielding. In contrast, compression along ED shows a pronounced increase in flow stress at approximately 8% true strain, indicating markedly different hardening behavior compared to the other two directions. The rapid work-hardening observed for ED compression of Mg extrusions has previously been reported by Chino *et al.* [20] and attributed to the formation of tensile twins. Moreover, when the results obtained at the three temperatures are compared, the flow stress decreases with increasing compression temperature for all loading directions (ED, TD, and ND).

In the VPSC simulation, the activity of each slip system, the crystallographic re-orientation caused by twinning, and

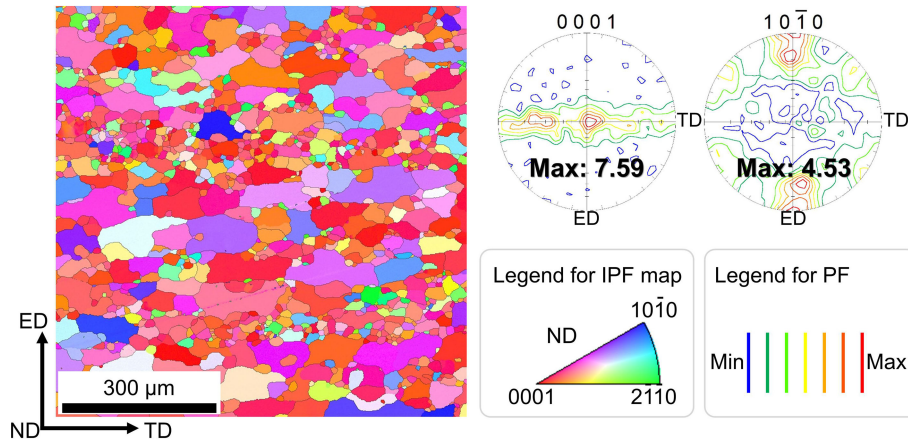


Fig. 1 EBSD IPF map and (0001) and (10 $\bar{1}$ 0) pole figures of AZ31B extruded plate. (online color)

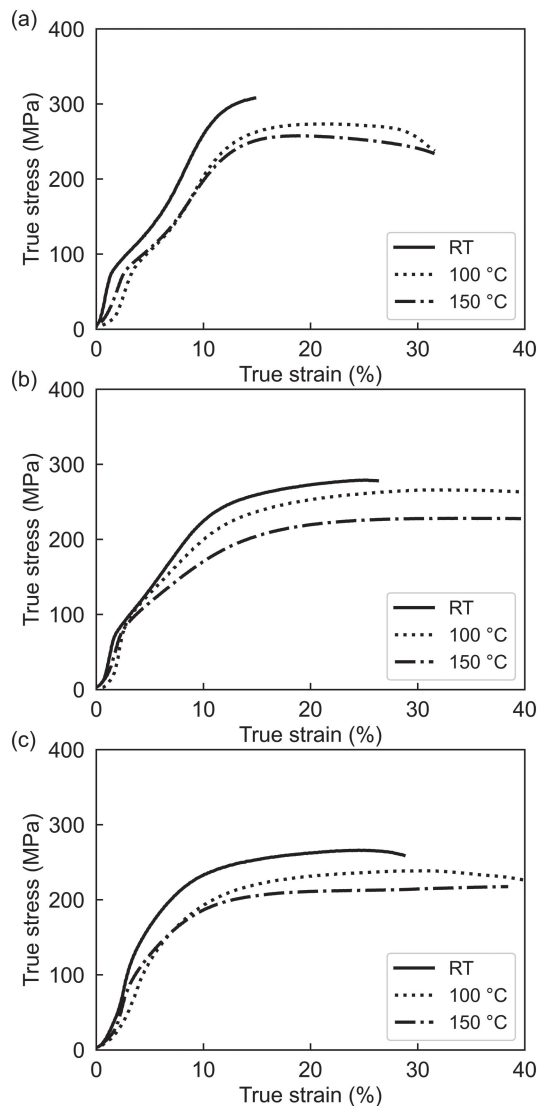


Fig. 2 True compression stress-strain curves of AZ31B extruded plate compressed along (a) ED, (b) TD and (c) ND at different temperatures.

the associated strain-hardening in each deformation mode are accounted for when calculating the macroscopic plastic response. Consequently, if dynamic recrystallization generates new grains during deformation, a discrepancy arises between the experimental situation and the assumptions of

the VPSC model. To verify whether dynamic recrystallization or grain-boundary sliding occurs under the present compression conditions, EBSD analyses were performed on the specimens compressed at 150°C.

Figure 3 displays the IPF maps (upper row) and the corresponding KAM maps (lower row) obtained after compression at 150°C for the three loading directions (ED, TD, and ND). The true compressive strains applied were 31% for ED, 39% for TD, and 38% for ND. In all three cases, the microstructures were dominated by highly deformed grains, and the KAM maps showed values exceeding 1° over the entire area. Such high KAM values indicate substantial plastic strain throughout the material, and the absence of regions with low misorientation suggests that no new recrystallized grains formed. Because the 150°C compression represents the highest temperature among the three conditions examined in this study, we can infer that dynamic recrystallization does not occur at any of the lower temperatures (room temperature and 100°C) either.

Specimens compressed at 100°C to true strains of 4.2% (ED), 4.0% (TD), and 4.1% (ND) were also examined by performing EBSD. This analysis confirmed that the twins generated during deformation were almost entirely tensile. At this deformation stage, the measured tensile-twin fractions were 39.1% for the ED-compressed sample, 19.4% for the TD-compressed sample, and 8.6% for the ND-compressed sample.

Mg alloys have been reported to exhibit grain-boundary sliding at relatively low temperatures compared to many other metallic systems [21, 22]. Because the VPSC framework accounts only for dislocation slip and twin-induced strain, the presence of pronounced grain-boundary sliding creates a discrepancy between experimental reality and the model assumptions. To verify whether grain boundary sliding occurred under our compression conditions, we employed the surface-marking technique based on high-voltage EBSD scanning proposed by Huang *et al.* [23]. Straight-line markings were inscribed on the specimen surface using an EBSD scan at an accelerating voltage of 29 kV, after which the specimens were compressed and examined using scanning electron microscopy (SEM) to observe any deformation of the markings. The specimens examined were those compressed to 13.6% strain along the ND at 150°C.



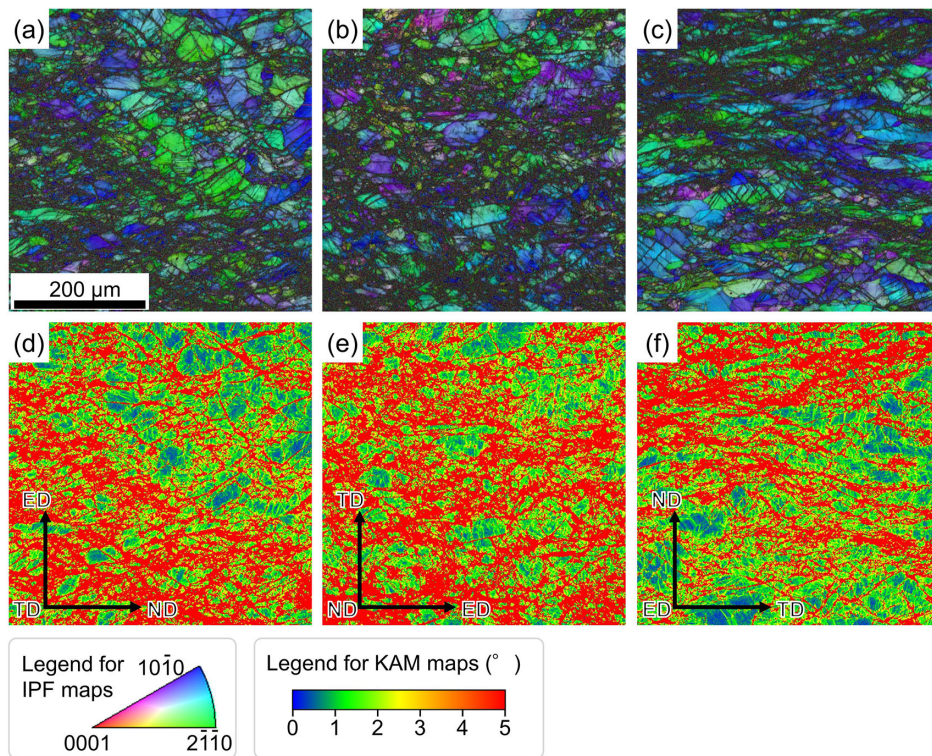


Fig. 3 EBSD IPF maps (a)–(c) and KAM maps (d)–(f) obtained from AZ31B extruded plate compressed along (a), (d) ED, (b), (e) TD and (c), (f) ND at 150°C. (online color)

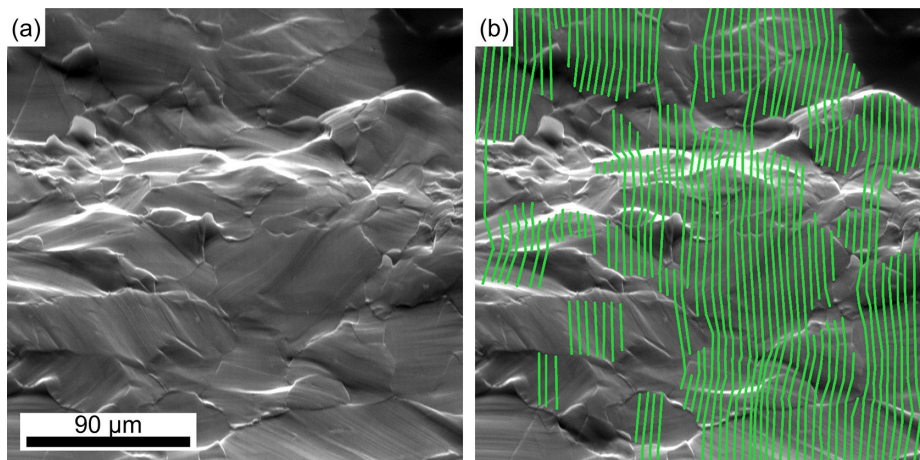


Fig. 4 (a) SEM image of the surface of AZ31B extruded plate compressed by 13.6% along ND. (b) corresponding image with highlighted surface marking. (online color)

Figure 4(a) shows an SEM image of the specimen surface after compression, whereas Fig. 4(b) highlights the same image with the EBSD-induced marking lines superimposed. The markings are observed to bend at grain boundaries owing to local strain incompatibility between adjacent grains. However, they remain continuous across all grain boundaries, indicating that no significant grain-boundary sliding is observed. Grain-boundary sliding is known to be grain-size dependent, occurring more readily in fine-grained materials [21]. The present specimens have an average grain size of  $46.9\text{ }\mu\text{m}$ , which is considerably coarser than the  $\approx 8\text{ }\mu\text{m}$  grains in which Koike *et al.* [22] reported grain-boundary sliding at room temperature. Therefore, we infer that grain-boundary sliding is absent in our experiments.

Based on the foregoing results, the deformation mechanisms operating in the AZ31B extruded plate during both the room-temperature and warm-compression tests can be attributed to dislocation slip together with the activity of tensile twins. In the present work, building on these experimental findings and on previous VPSC studies of Mg alloys [10, 12, 16, 17, 24], we performed VPSC simulations that explicitly included the following deformation modes: basal  $\langle a \rangle$  slip  $\{0002\}\langle 11\bar{2}0 \rangle$ , prismatic  $\langle a \rangle$  slip  $\{1\bar{1}00\}\langle 11\bar{2}0 \rangle$ , pyramidal II  $\langle c + a \rangle$  slip  $\{11\bar{2}2\}\langle 11\bar{2}\bar{3} \rangle$ , and tensile twinning  $\{10\bar{1}2\}\langle 10\bar{1}1 \rangle$ .

The set of Voce-hardening parameters may not be uniquely identifiable, depending on the condition; this can adversely affect the reliability of the analysis [8]. To evaluate the

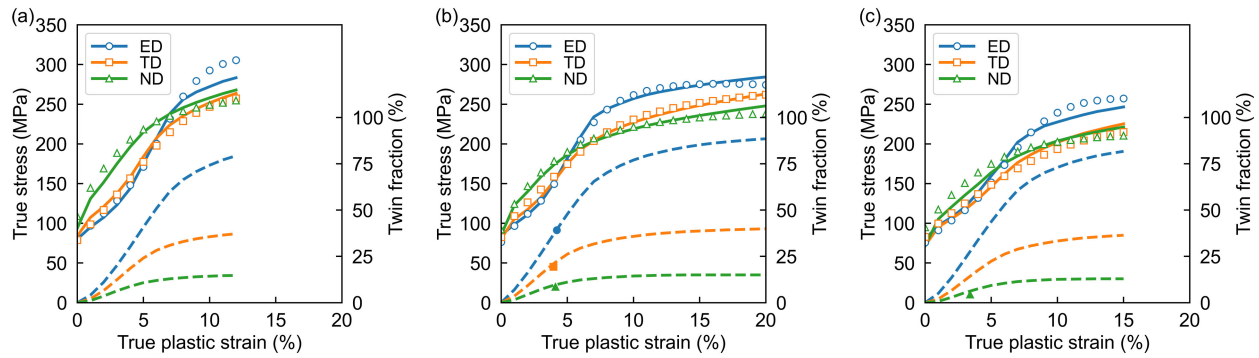


Fig. 5 Experimental and simulated true stress-strain and tensile twin fraction curves of AZ31B compressed at (a) RT, (b) 100°C, and (c) 150°C. Solid lines and open markers represent compression curves, and dotted lines and solid markers represent twinning fractions. In both cases, the markers represent experimental data, and the curves represent VPSC simulation results. (online color)

uniqueness of the fitted parameters and assess the robustness of the subsequent interpretation, 32 independent parameter identification runs were performed for each temperature. For the compression tests at room temperature, 100°C, and 150°C, successful fits—i.e., simulations that reproduced the experimental compression curves with comparable accuracy—were obtained in 19, 19, and 12 cases, respectively; the remaining runs failed to converge, resulting in simulated curves that deviated markedly from the measured data. Among the successful cases, the extracted parameter sets exhibited some scatter within each condition, resulting in modest variation in the predicted activity levels of the individual slip systems. Consequently, for each temperature, we selected the parameter set that yielded results closest to the mean of the successful repetitions and used these “representative” values for the subsequent analysis of critical resolved shear stresses and deformation-mode activities. A detailed discussion of parameter variability and its impact on analytical outcomes is provided in Appendix A1.

Figure 5 presents the VPSC simulation results for the compression curves at each temperature, together with the tensile-twin fractions measured for compressions along the ED, TD, and ND. The initial texture used in the simulations was taken from the EBSD data shown in Fig. 1; all 1,499 grains identified in the undeformed specimen were weighed according to their respective area fractions.

For each temperature, fitting was performed over a strain interval in which the deformation remained essentially homogeneous, and the influence of cracking could be neglected. Specifically, the fitting intervals were 0–12% true strain at room temperature, 0–20% at 100°C, and 0–15% at 150°C, as determined from the experimental compression curves. As shown in Fig. 5, the VPSC simulations reproduce the experimental compression curves very well at all three temperatures.

In addition, separate compression experiments were conducted at 100°C for the three loading directions (ED, TD, and ND) and at 150°C for ND compression. The tensile twin fractions obtained from these tests are plotted in the same figure. The twin fraction was determined by comparing the EBSD orientation maps obtained before and after deformation, marking the regions that exhibited the characteristic orientation change associated with tensile twinning using OIM Analysis 7.0, and then calculating the

area fraction of the marked regions. As shown in Fig. 5, the comparison between experimental measures and VPSC simulations reveals that the model accurately reproduces the evolution of tensile twin fractions across the investigated temperature range.

In the present analysis, the compression curves are the quantities fitted, meaning that the VPSC simulation can, in principle, reproduce the measured stress–strain response even if it does not capture the actual deformation mechanisms. Consequently, the credibility of the simulation results must be verified by comparing them with data not used in the fitting procedure. In this study, as per the recommendation of Hama *et al.* [25], who emphasized the importance of the strain component perpendicular to the loading direction for VPSC parameter fitting and considering the crystallographic texture commonly employed to verify the validity of VPSC parameters [8, 9, 15], we assessed the credibility of the simulation results.

Figure 6 shows a comparison between the VPSC-predicted strain component normal to the compression axis and the experimentally measured value for the same quantity. The experimental normal strain was obtained from the dimensional measurements of the specimens after the compression test. As shown in Fig. 6, when the specimen is compressed along the ED, the ratio of the normal strain to the axial strain remains close to 1:1 during the early stage of deformation (up to  $\approx 15\%$  true strain). In contrast, for compression along the TD or ND, this ratio deviates from unity at the onset of deformation, and the strain is consistently smaller for the ED than for the TD or ND. The extruded AZ31B plate employed in this work possesses the typical texture of Mg extrusions in which the basal planes are oriented normal to the ED (i.e., the ND–TD plane), as shown in Fig. 1; therefore, the observed differences reflect the influence of the initial texture.

No significant discrepancies were observed between the simulation and experiment, and the relative magnitudes of the strain components normal to the loading direction were reproduced for all three loading orientations. This confirms that the VPSC simulation can correctly predict plastic deformation behavior while incorporating the effect of the initial texture. Note that the curves plotted in Fig. 6 were calculated outside the strain interval employed for parameter fitting; thus, they represent an extrapolation of the strain. Nevertheless, for every loading condition, the experimentally



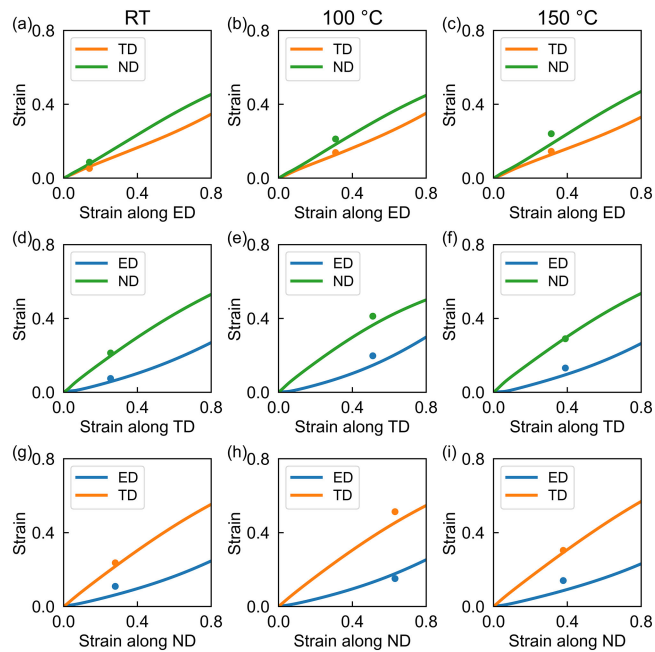


Fig. 6 Strain perpendicular to the compression axis when compressed along (a)–(c) ED, (d)–(f) TD and (g)–(i) ND at (a), (d), (g) RT, (b), (e), (h) 100°C and (c), (f), (i) 150°C. The curve indicates VPSC simulation result, the marker indicates experimental data. (online color)

measured normal strain was well reproduced by the VPSC model, indicating that the simulation possessed a certain degree of extrapolative capability.

Figure 7 presents a comparison of the textures obtained from EBSD for specimens that were compressed at 100°C to

true strains of 4.2% (ED), 4.0% (TD), and 4.1% (ND) with the textures predicted from the VPSC simulation for a 4.0% compression in each loading direction. In the (0001) pole figures, for all three compression directions, the fraction of orientations that lie closer to the compression axis increases relative to the initial texture, as shown in Fig. 1. By contrast, the fraction of orientations perpendicular to the compression axis decreases. This trend is consistent with the texture evolution expected from tensile twinning-induced crystallographic reorientation, as shown in Fig. 5(b). Even the ND-compressed specimen, despite having the lowest twin fraction, still contains 8.6% tensile twins; thus, the observed changes can be attributed primarily to their formation. Moreover, the experimental and simulated textures agreed well for both (0001) and  $10\bar{1}0$  pole figures, confirming that the VPSC model accurately reproduced the texture evolution induced by compression.

Thus, the VPSC simulation reproduces with high fidelity the strain component normal to the loading direction, the evolving texture, and the tensile-twin fractions at 100 and 150°C. The computational results can be considered to have a reasonable degree of validity for the deformation conditions and strain ranges examined in this study.

The Voce-hardening parameters obtained from the fitting are listed in Table 1. The corresponding threshold stresses for each deformation mode were calculated using Eq. (2). The results are shown in Fig. 8. In the figure, the vertical axis represents the threshold stress (i.e., the shear stress required to activate each deformation mode) and the horizontal axis corresponds to the total accumulated shear strain within a grain. The relative magnitudes of the threshold stresses

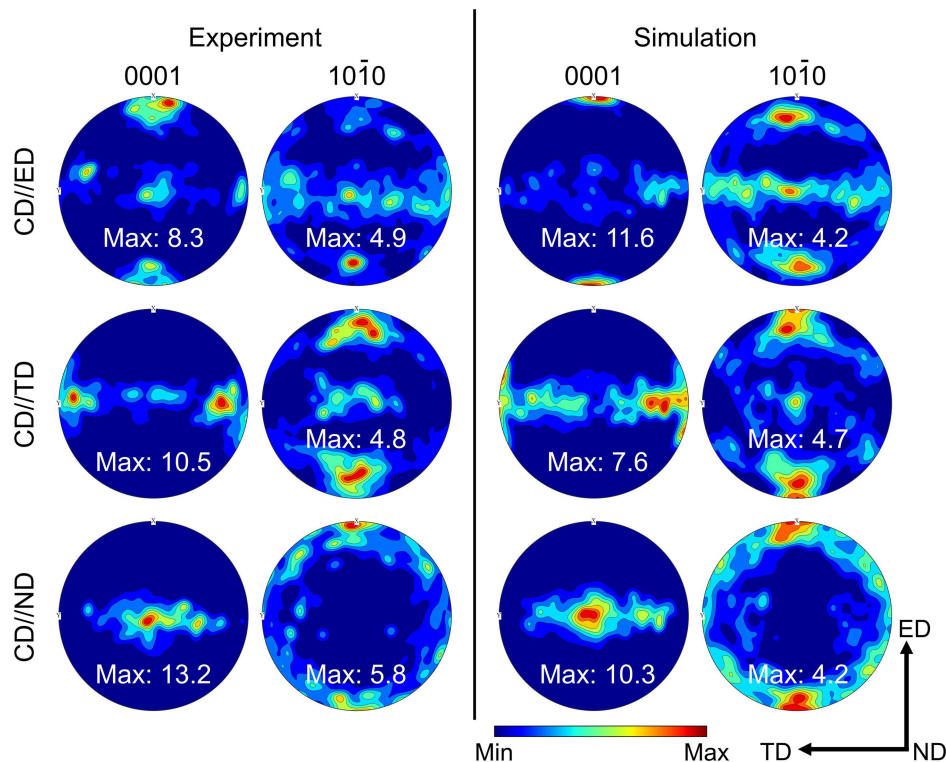


Fig. 7 Experimental and simulated textures of AZ31B samples compressed at 100°C along ED, TD and ND. Experimental data were measured at 4.2%, 4.0% and 4.1% deformation for ED, TD and ND compression samples, respectively. Data for the simulations were taken at 4.0% compression in all directions. (online color)

Table 1 The fitted Voce-hardening parameters of AZ31B at different temperatures.

Temperature	Mode	Voce-Hardening parameter (MPa)			
		$\tau_0$	$\tau_1$	$\theta_0$	$\theta_1$
RT	Basal<a>	21	7	4760	117
	Prismatic<a>	33	40	348	41
	Pyramidal<c+a>	114	24	8876	0
	Tensile twin	40	0	0	0
100 °C	Basal<a>	18	7	4136	101
	Prismatic<a>	40	20	261	59
	Pyramidal<c+a>	61	50	8249	0
	Tensile twin	38	0	0	0
150 °C	Basal<a>	27	3	5142	33
	Prismatic<a>	36	20	215	39
	Pyramidal<c+a>	64	52	7845	0
	Tensile twin	37	0	0	0

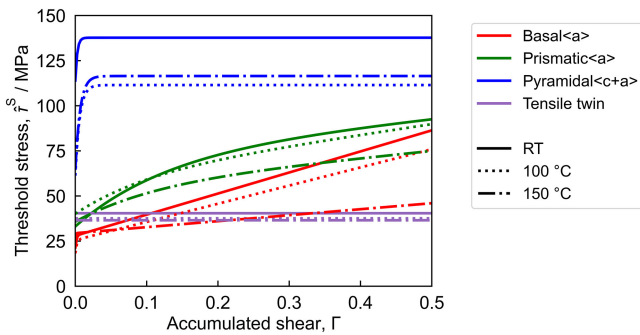


Fig. 8 Voce hardening curves of basal (a) slip, prismatic (a) slip, pyramidal (c + a) slip and tensile twinning of AZ31B at different temperatures. (online color)

follow the typical hierarchy observed for Mg alloys: basal (a) slip and tensile twinning have comparable values, prismatic (a) slip is somewhat higher, and pyramidal (c + a) slip is the highest, in agreement with the reported order of the CRSS for Mg alloys [4].  $\tau_0$  denotes the shear stress required to initiate each deformation mode in the undeformed state; however, it does not directly correspond to the CRSS measured in single crystals. This discrepancy arises because the threshold stresses in the VPSC simulation are effective values that

include grain-boundary strengthening and other microstructural effects, as previously reported by Raeisnia *et al.* [16]. Consequently, the  $\tau_0$  values estimated in the present work were larger than the CRSS values obtained from the single-crystal experiments for the respective deformation modes [26–28].

#### 4. Discussion

In this study, VPSC simulations were conducted to predict the compressive response of AZ31B at room temperature, 100°C, and 150°C. The simulated compression curves and threshold stresses of the individual deformation modes were extracted for each temperature and compression direction. In the subsequent sections, these results are compared with the deformation-mode activity levels obtained from the VPSC calculations, and the inter-relationships among the observed deformation behavior, slip-system activity, and the corresponding threshold stresses are discussed.

##### 4.1 Influence of compression direction

Figure 9 displays the relative activity of individual deformation modes as predicted by the VPSC simulations. The vertical axis represents the fraction of total shear deformation accommodated by a given deformation mode,

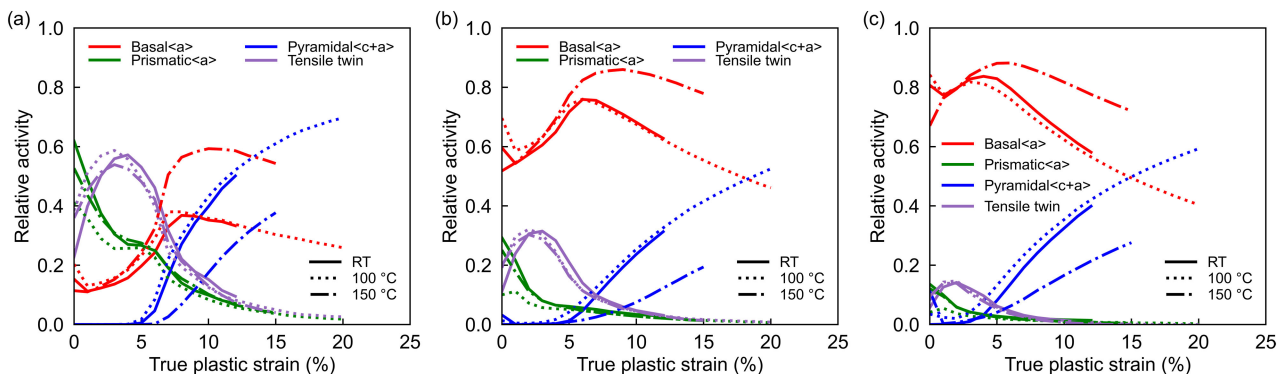


Fig. 9 Relative activities of basal (a) slip, prismatic (a) slip, pyramidal (c + a) slip and tensile twinning during compression of AZ31B along (a) ED, (b) TD and (c) ND at different temperatures. (online color)

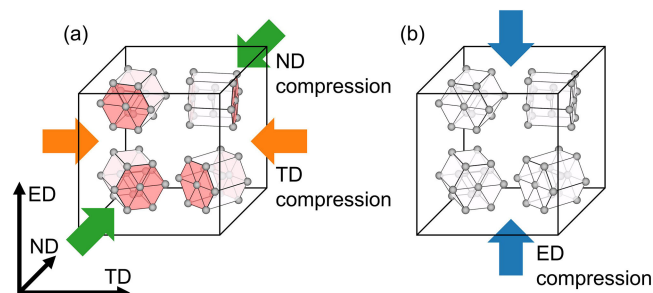


Fig. 10 Schematic representation of the relationship between the orientation of basal plane and the direction of compression of (a) TD, ND and (b) ED. (online color)

while the horizontal axis corresponds to the true plastic strain. Figures 9(a)–9(c) show the results for compression along the ED, TD, and ND, respectively. In each panel, the deformation behavior at room temperature, 100°C, and 150°C is plotted together.

Overall, the activity of each deformation mode varied with both the compression temperature and direction, with the latter exerting a powerful influence. When the compression axis was parallel to the ED (Fig. 9(a)), tensile twinning and prismatic  $\langle a \rangle$  slip dominate in the early stage (up to  $\approx 5\%$  true strain), whereas at larger strains ( $\approx 5\text{--}7\%$  and beyond) the contributions of basal  $\langle a \rangle$  slip and pyramidal  $\langle c + a \rangle$  slip increase. The prominent activation of tensile twins in the early stages of ED compression of Mg extrusions is a universal behavior that has already been reported in VPSC simulations of Mg–Al–Mn alloys by Bian *et al.* [11] and confirmed experimentally by Chino *et al.* [20, 29].

In contrast, when the compression axis is the TD or the ND, basal  $\langle a \rangle$  slip remains the dominant deformation mode throughout the deformation at all temperatures. In addition, during the early stage of deformation (plastic strain up to roughly 5–7%), prismatic  $\langle a \rangle$  slip and tensile twinning are active, whereas at larger strains (greater than about 5–7%), pyramidal  $\langle c + a \rangle$  slip becomes operative. These differences can be ascribed to the initial crystallographic textures of the AZ31B specimens used in this study. The texture of the extruded material is typical of Mg extrusion, in which the basal planes are oriented perpendicular to the ED. Accordingly, as shown in Fig. 10(a), many grains have their basal planes inclined approximately 45° with respect to the compression axis during TD or ND compression, allowing basal  $\langle a \rangle$  slip to be readily activated. By contrast, as shown in Fig. 10(b), in compression along the ED, the basal planes of most grains are nearly orthogonal to the loading axis, making basal  $\langle a \rangle$  slip difficult and leading to a relative increase in the activity of other deformation modes with higher critical resolved shear stresses.

As shown in Fig. 2, the difference in mechanical response between the two directions (TD and ND) and the ED is also reflected in the compression curves: for compression along the ED, the material exhibits a pronounced work-hardening after roughly 6% true strain, which manifests as a rapid rise in flow stress. When the activity of each deformation mode during ED compression (Fig. 9(a)) is examined, in the strain range where this work-hardening recovery occurs (around 7% true strain), the dominant deformation mechanism

switches from prismatic  $\langle a \rangle$  slip together with tensile twinning to basal  $\langle a \rangle$  slip and pyramidal  $\langle c + a \rangle$  slip. A similar recovery of work hardening associated with a change in the active deformation modes [30] was reported for the tensile deformation of ultrafine-grained Mg alloys by Zheng *et al.* [31] and is regarded as a promising route for combining high strength with high ductility. The AZ31B extruded material used in the present study has a relatively coarse grain size (average 46.9  $\mu\text{m}$ ); therefore, the activation of multiple slip systems cannot be attributed to grain-size effects. Moreover, the VPSC simulations, which incorporate both slip activity and the crystallographic rotation induced by tensile twinning, successfully reproduce this behavior, indicating that the observed change in active deformation modes originates from the crystallographic re-orientation caused by slip and twinning. Consequently, these results suggest that appropriately controlling the initial texture can help exploit the rotation of grain orientations to simultaneously activate several deformation modes, offering a novel approach for achieving a combination of high strength and ductility in Mg alloys.

#### 4.2 Influence of compression temperature

In the temperature range from room temperature up to 150°C, the activity of each slip system changes with increasing temperature, depending on the specific temperature interval (indicated by the solid, dashed, and dash-dot lines in Fig. 9). Specifically, when the temperature is raised from room temperature to 100°C, the activity of pyramidal  $\langle c + a \rangle$  slip increases slightly for all compression directions, whereas the activities of the other slip systems remain essentially unchanged or decrease. Conversely, when the temperature is further increased from 100 to 150°C, the activities of basal  $\langle a \rangle$  slip and prismatic  $\langle a \rangle$  slip become higher. In the VPSC simulation, the difference in compression temperature was ultimately reflected in the Voce-hardening parameters of each deformation mode, namely the corresponding threshold stresses. Therefore, the observed variations can be ascribed to temperature-dependent changes in the threshold stresses, which are examined in detail below.

First, for the temperature interval between room temperature and 100°C, the threshold stresses of the individual deformation modes displayed in Fig. 8 were examined. The threshold stress of the pyramidal  $\langle c + a \rangle$  slip decreased by roughly 20 MPa when the temperature was raised from room temperature to 100°C, whereas the other three deformation modes showed only minor changes. Hence, in the range of room temperature to 100°C, the pronounced softening of the pyramidal  $\langle c + a \rangle$  slip, relative to the other modes, is considered to be responsible for the increase in its relative activity.

Similarly, when the temperature was increased from 100 to 150°C, the threshold stresses of pyramidal  $\langle c + a \rangle$  slip and tensile twinning remain essentially unchanged, whereas those of basal  $\langle a \rangle$  slip and prismatic  $\langle a \rangle$  slip decrease markedly (Fig. 8). Consequently, the activity of basal  $\langle a \rangle$  slip and prismatic  $\langle a \rangle$  slip becomes relatively higher in the 100–150°C interval. Note that despite a temperature rise of 50°C, the threshold stress of pyramidal  $\langle c + a \rangle$  slip exhibited only a minimal variation. In most Mg alloys, increasing temperature



reduces the CRSS of non-basal slip systems, making them easier to activate [3]. However, for pure Mg, the CRSS of  $\langle c + a \rangle$  pyramidal slip reaches a maximum near the sub-warm region around 100°C [32]. Therefore, the negligible change in the pyramidal  $\langle c + a \rangle$  slip threshold observed between 100 and 150°C is likely because its CRSS lies near this maximum, where temperature has little effect.

## 5. Conclusions

In this study, the extruded AZ31B alloy was examined by performing VPSC simulations to investigate slip-system activity during warm compression in the scarcely reported sub-warm temperature range of 100–150°C. The following conclusions were drawn:

- (1) No evidence of pronounced dynamic recrystallization or of grain-boundary sliding was found in the specimens compressed at 150°C. Consequently, over the entire temperature interval up to 150°C, the dominant deformation mechanisms are dislocation slip and tensile-twin activity.
- (2) For compression parallel to the ED, an abrupt increase in work-hardening occurred at a true plastic strain of about 6% at all temperatures, coinciding with a switch in the prevailing deformation mode. Beyond a true strain of roughly 7%, the activity of basal  $\langle a \rangle$  slip and pyramidal  $\langle c + a \rangle$  slip increases markedly.
- (3) When the compression axis is TD or ND, basal  $\langle a \rangle$  slip dominates throughout deformation at all temperatures. In the early stage of deformation (true strain  $\leq 5\text{--}7\%$ ), prismatic  $\langle a \rangle$  slip and tensile twinning are also active, whereas at larger strains (true strain  $> 5\text{--}7\%$ ), pyramidal  $\langle c + a \rangle$  slip becomes operative.
- (4) Quantitative analysis of the slip system activity revealed that the effect of increasing the compression temperature on the relative activity of each deformation mode depends on the temperature interval. Specifically, raising the temperature from room temperature to 100°C enhances the activity of pyramidal  $\langle c + a \rangle$  slip, whereas further heating from 100 to 150°C promotes the activity of basal  $\langle a \rangle$  slip and prismatic  $\langle a \rangle$  slip.
- (5) In the 100–150°C interval, the critical resolved shear stress (threshold stress) of pyramidal  $\langle c + a \rangle$  slip changes only marginally. This behavior is attributed to the maximum of the CRSS of pyramidal  $\langle c + a \rangle$  slip in pure Mg that occurs around 100°C.

## Acknowledgement

The work presented in this paper is based on results obtained at the Sectional meeting on common-use, high-performance, and high-reliability magnesium alloys of The Japan Institute of Light Metals. We would like to express our sincere gratitude to all committee members for their valuable support.

## REFERENCES

- [1] H. Mori, K. Fujino, K. Kurita, Y. Chino, N. Saito, M. Noda, H. Komai and H. Obara: Application of the Flame-Retardant Magnesium Alloy to High Speed Rail Vehicles, *Materia Japan* **52** (2013) 484–490.
- [2] S. Takeda: Technical Trends of Magnesium Die-casting for Automobile Parts, *Materia Japan* **53** (2014) 594–598.
- [3] H. Yoshinaga: Crystal plasticity of magnesium, *Keikinzoku/J. JILM* **59** (2009) 450–457.
- [4] J. Koike: Deformation mechanisms of magnesium alloys at ambient temperature, *Keikinzoku/J. JILM* **59** (2009) 272–277.
- [5] K. Manabe: Sheet and tube forming processing of magnesium, *Keikinzoku/J. JILM* **60** (2010) 41–51.
- [6] J. Kaneko and M. Sugamata: Mechanical properties and formability of magnesium alloy sheets, *Keikinzoku/J. JILM* **54** (2004) 484–492.
- [7] M. Sato: Rolling Process of Magnesium Alloy and their Application, *J. JSTP* **48** (2007) 373–378.
- [8] A. Chapuis and Q. Liu: Investigating the temperature dependency of plastic deformation in a Mg–3Al–1Zn alloy, *Mater. Sci. Eng. A* **725** (2018) 108–118.
- [9] A. Jain and S.R. Agnew: Modeling the temperature dependent effect of twinning on the behavior of magnesium alloy AZ31B sheet, *Mater. Sci. Eng. A* **462** (2007) 29–36.
- [10] Y. Matsuoka, M. Bian, X. Huang, Y. Tsukada, T. Koyama and Y. Chino: Simulation-aided analysis on mechanical properties of dilute Mg–Zn–Ca alloy sheets, *J. Alloy. Compd.* **906** (2022) 164285.
- [11] M.Z. Bian, A. Tripathi, H. Yu, N.D. Nam and L.M. Yan: Effect of aluminum content on the texture and mechanical behavior of Mg–1 wt% Mn wrought magnesium alloys, *Mater. Sci. Eng. A* **639** (2015) 320–326.
- [12] M. Bian, X. Huang and Y. Chino: A combined experimental and numerical study on room temperature formable magnesium–silver–calcium alloys, *J. Alloy. Compd.* **834** (2020) 155017.
- [13] S.R. Agnew, M.H. Yoo and C.N. Tome: Application of texture simulation to understanding mechanical behavior of Mg and solid solution alloys containing Li or Y, *Acta Mater.* **49** (2001) 4277–4289.
- [14] R.A. Lebensohn and C.N. Tome: A self-consistent anisotropic approach for the simulation of plastic deformation and texture development of polycrystals: Application to zirconium alloys, *Acta Metall. Mater.* **41** (1993) 2611–2624.
- [15] G. Zhou, M.K. Jain, P. Wu, Y. Shao, D. Li and Y. Peng: Experiment and crystal plasticity analysis on plastic deformation of AZ31B Mg alloy sheet under intermediate temperatures: How deformation mechanisms evolve, *Int. J. Plast.* **79** (2016) 19–47.
- [16] B. Raeisnia, S.R. Agnew and A. Akhtar: Incorporation of Solid Solution Alloying Effects into Polycrystal Modeling of Mg Alloys, *Metall. Mater. Trans. A* **42** (2011) 1418–1430.
- [17] H. Wang, B. Raeisnia, P.D. Wu, S.R. Agnew and C.N. Tome: Evaluation of self-consistent polycrystal plasticity models for magnesium alloy AZ31B sheet, *Int. J. Solids Struct.* **47** (2010) 2905–2917.
- [18] C. Tome, G.R. Canova, U.F. Kocks, N. Christodoulou and J.J. Jonas: The relation between macroscopic and microscopic strain hardening in F.C.C. polycrystals, *Acta Metall.* **32** (1984) 1637–1653.
- [19] C.N. Tome, R.A. Lebensohn and U.F. Kocks: A model for texture development dominated by deformation twinning: Application to zirconium alloys, *Acta Metall. Mater.* **39** (1991) 2667–2680.
- [20] Y. Chino, K. Kimura, M. Hakamada and M. Mabuchi: Mechanical anisotropy due to twinning in an extruded AZ31 Mg alloy, *Mater. Sci. Eng. A* **485** (2008) 311–317.
- [21] M.G. Zelin, H.S. Yang, R.Z. Valiev and A.K. Mukherjee: Interaction of high-temperature deformation mechanisms in a Magnesium Alloy with Mixed Fine and Coarse Grains, *Metall. Trans. A* **23** (1992) 3135–3140.
- [22] J. Koike, R. Ohyama, T. Kobayashi, M. Suzuki and K. Maruyama: Grain-Boundary Sliding in AZ31 Magnesium Alloys at Room Temperature to 523 K, *Mater. Trans.* **44** (2003) 445–451.
- [23] Y.H. Huang, S.W. Xu, W.N. Tang and J.F. Nie: A new nano-scale surface marking technique for the deformation analysis of Mg-based alloys, *J. Magnes. Alloy.* **10** (2022) 2398–2403.
- [24] T. Ebeling, C. Hartig, T. Laser and R. Bormann: Material law parameter determination of magnesium alloys, *Mater. Sci. Eng. A* **527** (2009) 272–280.
- [25] T. Hama, Y. Tanaka, M. Uratani and H. Takuda: Deformation behavior upon two-step loading in a magnesium alloy sheet, *Int. J. Plast.* **82** (2016) 283–304.

- [26] H. Conrad and W.D. Robertson: Effect of temperature on the flow stress and strain-hardening coefficient of magnesium single crystals, *JOM* **9** (1957) 503–512.
- [27] R.E. Reed-Hill and W.D. Robertson: Deformation of magnesium single crystals by nonbasal slip, *JOM* **9** (1957) 496–502.
- [28] T. Obara, H. Yoshinga and S. Morozumi: {1122}⟨1123⟩ Slip system in magnesium, *Acta Metall.* **21** (1973) 845–853.
- [29] Y.N. Wang and J.C. Huang: The role of twinning and untwinning in yielding behavior in hot-extruded Mg–Al–Zn alloy, *Acta Mater.* **55** (2007) 897–905.
- [30] N. Tsuji, T. Shimokawa, K. Shizawa and M. Murayama: Realizing Structural Metallic Materials with Both High Strength and Large Ductility through Nucleation Control of Different Deformation Modes, *Materia Japan* **60** (2021) 8–12.
- [31] R. Zheng, T. Bhattacharjee, S. Gao, W. Gong, A. Shibata, T. Sasaki, K. Hono and N. Tsuji: Change of Deformation Mechanisms Leading to High Strength and Large Ductility in Mg–Zn–Zr–Ca Alloy with Fully Recrystallized Ultrafine Grained Microstructures, *Sci. Rep.* **9** (2019) 11702.
- [32] P.J.F. Stohr and J.P. Poirier: Etude en microscopie electronique du glissement pyramidal {1122}⟨1123⟩ dans le magnésium, *Philos. Mag.* **25** (1972) 1313–1329.

## Appendix

### A.1 Variability of estimated parameters and its impact on analysis results

Figure A1 shows the mean and standard deviation of the compression curves that correspond to the successful parameter estimations (19 cases at room temperature, 19 cases at 100°C, and 12 cases at 150°C), each of which reproduced the experimental compression curves with comparable accuracy. For each temperature and compression direction, the standard deviations of the simulated compression curves were relatively small, indicating that the simulated curves were close to the experimental data under all conditions. Noteworthy that even for the tensile-twin fraction—which was not employed in the fitting—the calculations obtained with the parameter sets that successfully reproduced the compression curves agree well with the measured values. This demonstrates that within the parameter range identified in the present work, the VPSC simulation can correctly capture plastic deformation behavior during compression.

Figure A2 displays, for the critical (threshold) stresses, the mean values and standard deviations obtained from the

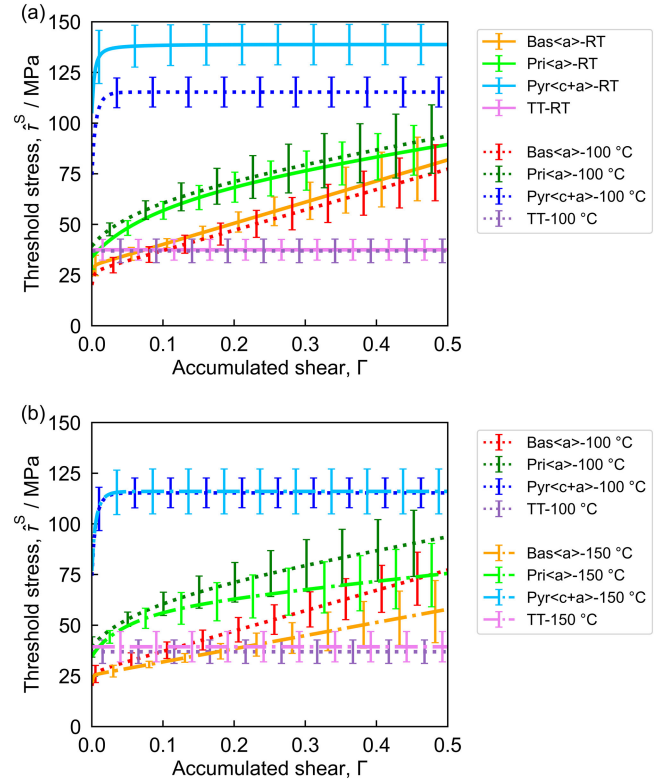


Fig. A2 Voce hardening curves of basal (a) slip (Bas(a)), prismatic (a) slip (Pri(a)), pyramidal (c + a) slip (Pri(c + a)) and tensile twinning (TT) of AZ31B at (a) RT and 100°C and (b) 100°C and 150°C. The mean and standard deviation of the results for multiple successful parameter estimations in each temperature are shown. (online color)

multiple successful parameter-estimation runs, in the same manner as Fig. A1. For ease of viewing, the data are presented in two separate panels: one comparing the room-temperature and 100-°C results, and the other comparing the 100-°C and 150-°C results.

The standard deviation of the threshold stresses can reach approximately 15 MPa, depending on the conditions, indicating a certain degree of scatter among the fitted parameter sets. Because the compression curves shown in Fig. A1 exhibit minimal standard deviations for all loading directions and temperatures, this observation implies that different parameter sets can essentially reproduce the same

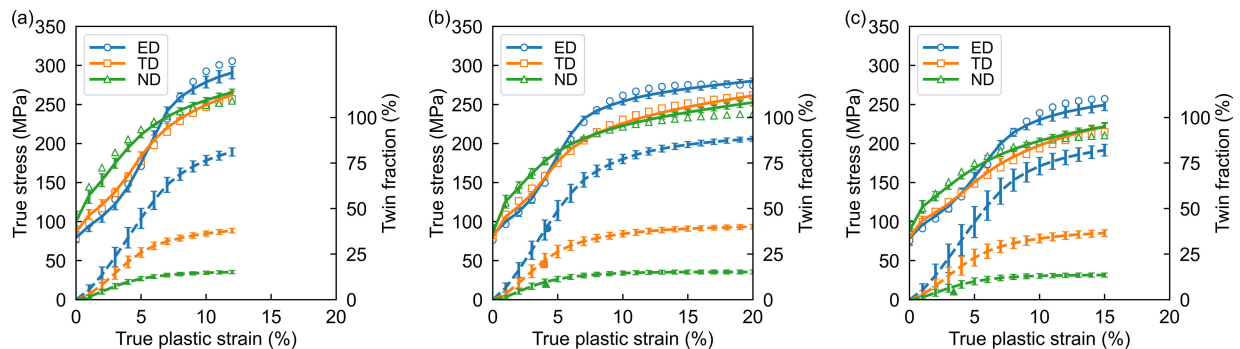


Fig. A1 Experimental and simulated true stress-strain and tensile twin fraction curves of AZ31B compressed at (a) RT, (b) 100°C, and (c) 150°C. Solid lines and open markers represent compression curves, and dotted lines and solid markers represent twinning fractions. In both cases, the markers represent experimental data, and the curves represent VPSC simulation results. For the simulation results, the mean and standard deviation of the results for multiple successful parameter estimations in each temperature are shown. (online color)

compression response. Consequently, when extracting reliable threshold stress information from the VPSC analyses, the variability illustrated here must be considered.

In the present work the trends discussed in the Results and Discussion—namely, (i) a reduction of the pyramidal  $\langle c + a \rangle$  slip threshold when the temperature is raised from room temperature to 100°C, and (ii) a reduction of the basal  $\langle a \rangle$  and

prismatic  $\langle a \rangle$  slip thresholds when the temperature is raised from 100 to 150°C, while the pyramidal  $\langle c + a \rangle$  threshold remains essentially unchanged—are also clearly observable from the mean values and their standard deviations shown in Fig. A2.

Figures A3 and A4 present the mean values and standard deviations of the relative activity obtained from multiple

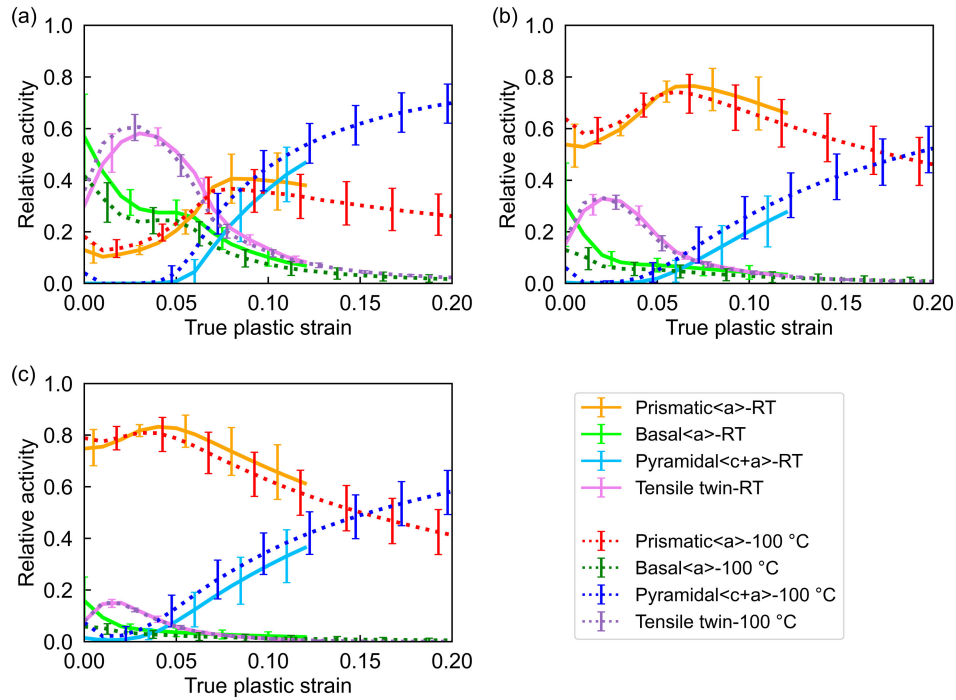


Fig. A3 Relative activities of basal  $\langle a \rangle$  slip, prismatic  $\langle a \rangle$  slip, pyramidal  $\langle c + a \rangle$  slip and tensile twinning during compression of AZ31B along (a) ED, (b) TD and (c) ND at RT and 100°C. The mean and standard deviation of the results for multiple successful parameter estimations in each temperature are shown. (online color)

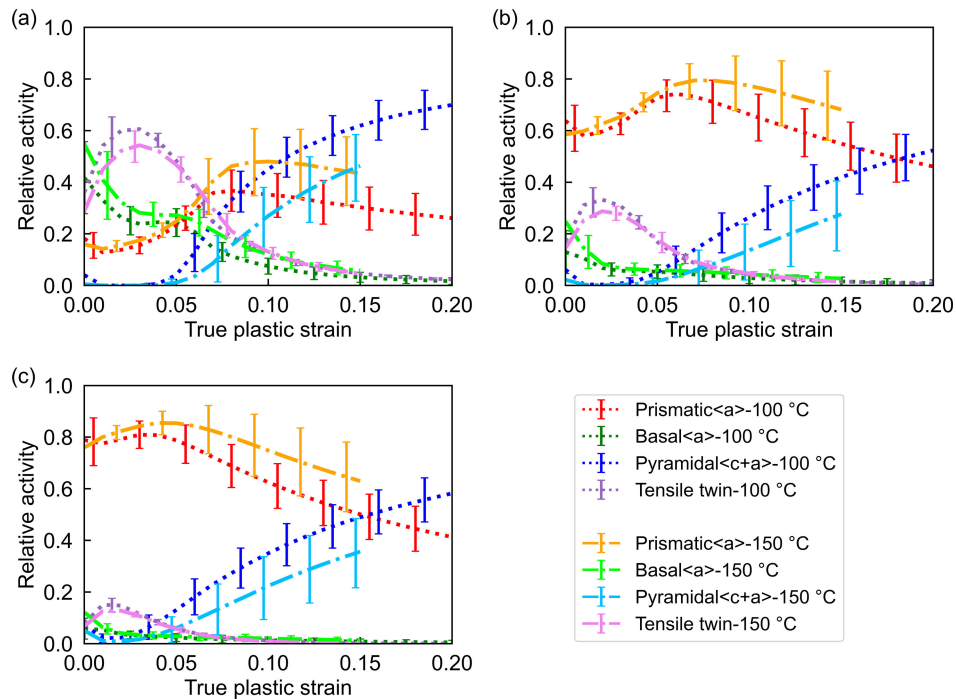


Fig. A4 Relative activities of basal  $\langle a \rangle$  slip, prismatic  $\langle a \rangle$  slip, pyramidal  $\langle c + a \rangle$  slip and tensile twinning during compression of AZ31B along (a) ED, (b) TD and (c) ND at 100°C and 150°C. The mean and standard deviation of the results for multiple successful parameter estimations in each temperature are shown. (online color)



successful parameter estimation runs for each deformation mode. As presented in Fig. A2, the data are split for clarity. Figure A3 presents a comparison of the results for the temperature interval of room temperature to 100°C, whereas Fig. A4 shows a comparison of the results for 100 to 150°C.

The scatter observed in the threshold stresses (Fig. A2) was also reflected in the activity levels; the standard deviation of the relative activity reached approximately 0.15. However, this variability is considerably smaller than the differences in tensile-twin activity among the various compression directions that were discussed in the main text, indicating that the conclusions regarding direction-dependent twin activity are not substantially affected by the parameter scatter.

Similarly, the more subtle temperature-dependent changes—namely the slight increase in pyramidal  $\langle c + a \rangle$  slip activity when the temperature is raised from room temperature to 100°C, and the increase in basal  $\langle a \rangle$  and prismatic  $\langle a \rangle$  slip activity (accompanied by a decrease in pyramidal  $\langle c + a \rangle$  slip activity) when the temperature is

raised from 100 to 150°C—are also evident in Figs. A3 and A4. Although these trends show some dependence on the compression direction and strain level, the overall trends are clearly evident in the figures. The magnitude of the activity-level scatter does not materially affect the conclusions presented in the main discussion.

In the present analysis, markedly different sets of parameters (i.e., threshold stresses) yielded virtually identical compression curves, indicating that derived quantities, such as slip-system activity, are also sensitive to the chosen parameter set. Under these circumstances, conventional manual trial-and-error fitting is prone to operator bias. To obtain reliable information on the threshold stresses and the activity of deformation modes from VPSC simulations, it is essential to eliminate this bias. The automated fitting procedure employed in this study, together with the systematic quantification of scatter across multiple independent estimations, provides a robust approach for extracting reliable data from VPSC simulations.